Exploring the possibilities of increasing energy density and efficiency in rechargeable batteries

Download this complimentary article collection

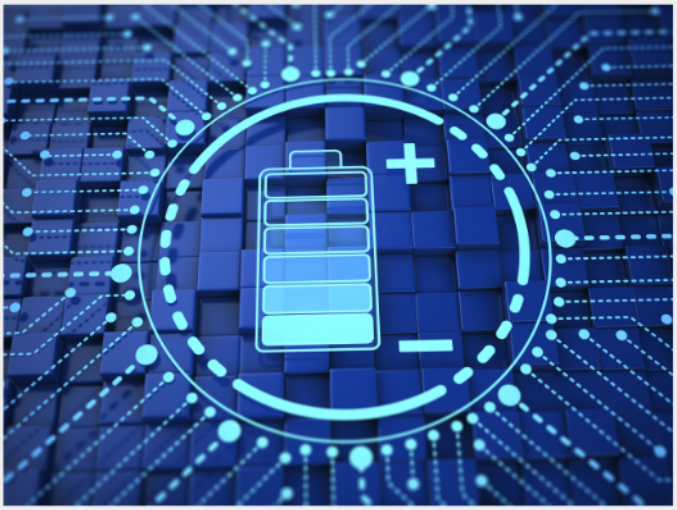

The exponential rise in the need for better, more efficient power sources has sparked an incredible amount of research into batteries. A primary focus of research has been increasing the energy density of batteries, as it allows for lighter, more portable storage of energy. Lithium-ion batteries, for example, have a much higher energy density than conventional lead-acid batteries and can be used for various purposes, such as in electric vehicles.

This article collection provides a comprehensive list of references for new methods and technologies for increasing the energy density of batteries.

Metrohm

WILEY

ADVANCED FUNCTIONAL MATERIALS
www.afm-journal.de

Untangling the Fundamental Electronic Origins of Non-Local Electron–Phonon Coupling in Organic Semiconductors

Peter A. Banks, Gabriele D'Avino, Guillaume Schweicher,* Jeff Armstrong, Christian Ruzié, Jong Won Chung, Jeong-Il Park, Chizuru Sawabe, Toshihiro Okamoto, Jun Takeya, Henning Sirringhaus, and Michael T. Ruggiero**

Organic semiconductors with distinct molecular properties and large carrier mobilities are constantly developed in attempt to produce highly-efficient electronic materials. Recently, designer molecules with unique structural modifications have been expressly developed to suppress molecular motions in the solid state that arise from low-energy phonon modes, which uniquely limit carrier mobilities through electron–phonon coupling. However, such low-frequency vibrational dynamics often involve complex molecular dynamics, making comprehension of the underlying electronic origins of electron–phonon coupling difficult. In this study, first a mode-resolved picture of electron–phonon coupling in a series of materials that are specifically designed to suppress detrimental vibrational effects, is generated. From this foundation, a method is developed based on the crystalline orbital Hamiltonian population (COHP) analyses to resolve the origins—down to the single atomic-orbital scale—of surprisingly large electron–phonon coupling constants of particular vibrations, explicitly detailing the manner in which the intermolecular wavefunction overlap is perturbed. Overall, this approach provides a comprehensive explanation into the unexpected effects of less-commonly studied molecular vibrations, revealing new aspects of molecular design that should be considered for creating improved organic semiconducting materials.

1. Introduction

Organic semiconductors have been the subject of immense study over the last few decades, as they can be processed in a variety of different manners for advanced applications ranging from flexible electronics to translucent photovoltaics.[1–3] These materials, which often contain highly-conjugated molecular subunits, can be readily synthesized from solution and are easily cast into 67thin films, opening the door for countless fabrication methods and ultimate use cases.[4–8] However, widespread application of organic semiconducting materials is primarily impeded by the low charge-carrier mobilities that they exhibit – typically on the scale of 0.1–20 $cm^2\ V^{-1}\ s^{-1}$—which fail to compete with inorganic semiconductors that have mobilities on the scale of 10^3–10^5 $cm^2\ V^{-1}\ s^{-1}$.[9–11] While the exact mechanism of charge transport in organic semiconductors remains a topic of debate, designing new materials with improved charge-carrier mobilities is a critical and highly-active area of study.[12–30]

P. A. Banks, M. T. Ruggiero
Department of Chemistry, University of Vermont
82 University Place
Burlington Vermont 05405, USA
E-mail: Michael.Ruggiero@uvm.edu

G. D'Avino
Grenoble Alpes University, CNRS, Grenoble INP, Institut Néel
38042 Grenoble, France
E-mail: gabriele.davino@neel.cnrs.fr

G. Schweicher, C. Ruzié
Laboratoire de Chimie des Polymres, Facult des Sciences
Universit Libre de Bruxelles (ULB)
Boulevard du Triomphe, CP 206/01, Bruxelles 1050, Belgium
E-mail: Guillaume.Schweicher@ulb.be

J. Armstrong
ISIS Facility, Rutherford Appleton Laboratory
Harwell Oxford, Didcot
Oxfordshire OX11 0QX, UK

J. W. Chung, J.-I. Park
Organic Material Lab.
Samsung Advanced Institute of Technology (SAIT), Samsung Electronics
Suwon 16678, South Korea

The ORCID identification number(s) for the author(s) of this article can be found under https://doi.org/10.1002/adfm.202303701

DOI: 10.1002/adfm.202303701

A variety of factors play a role on dictating charge-carrier mobility, including the electronic structure of the material, molecular packing, and detrimental effects such as electron–phonon coupling, to name a few.[9,10] The latter is particularly relevant for organic semiconductors, as these weakly-bonded van der Waals solids are well-known to exhibit a rich set of low-frequency vibrational dynamics (1–100 cm^{-1}, 0.03–3 THz, 0.12–12.4 meV) that are highly-excited at ambient temperatures – precisely the modes responsible for well-known thermal energetic disorder in organic semiconductors.[9,10,31–34] But, while electronic structure and electron–phonon coupling are often investigated and optimized in isolation, it is crucial to consider them simultaneously, as they are inextricably linked. For example, in many cases, chemical alterations to the molecular subunits will result in 1) a new crystalline packing geometry, 2) modified electronic structure, and 3) a new set of low-energy vibrational dynamics—making holistic comprehension of molecular design a priori a challenging task.

In a recent report, we have demonstrated the ability to determine a mode-resolved picture of electron–phonon coupling in crystalline organic semiconductors, using a combination of experimental low-energy vibrational spectroscopy and periodic density functional theory (DFT) simulations.[18] This method successfully enabled a means to accurately determine carrier mobilities from first-principles, primarily highlighting the specific molecular displacements that were most responsible for detrimental electron–phonon coupling. However, while this approach was able to identify these motions, the underlying atomic-scale origins of their harmful effects remain enigmatic. Such comprehension is crucial for the design of new materials, as the ability to pinpoint the exact modulations of inter-atomic—or even inter-orbital—interactions that ultimately obstruct charge-carrier transport will enable more precise molecular design, expediting the discovery of new materials.

In this work, we extend our previous mode-resolved electron–phonon coupling methodology to the next generation of organic semiconductors—in some cases considering materials that were specifically designed to suppress detrimental motions.[12,24,35] Subsequently, we investigate the role of lattice dynamics on the modulation of intermolecular orbital overlap, with a resolution that takes into consideration contributions from single atomic wavefuntions. This enables pinpointing the exact interatomic electronic interactions that most strongly contribute to the electron–phonon coupling constants, highlighting the areas of the individual molecules that drive the bulk semiconducting behavior of these materials. Additionally, because the distinct molecular modifications of the systems investigated here result in unique sets of low-frequency vibrational dynamics, this rigorous approach further uncovers how less-commonly studied and system-specific complex mode-types uniquely limit charge transport. Such a methodology and understanding provides valuable insight that will further aid the design of new and improved materials.

2. Results and Discussion

There are an increasing number of reports that have found that low-frequency (THz) vibrations in organic semiconducting molecular crystals are the primary driver of detrimental energetic disorder, with new materials regularly reported in the literature that were synthesized to suppress such effects.[18–20,36] In this work, we have initially extended our previously-reported mode-resolved electron–phonon coupling method to some of the most current highest-performance organic semiconducting materials: C6-DNT-VW (3,9-dihexyldinaphtho[2,3-*b*:2′,3′-*d*]-thiophene), C10-DNBDT-NW (3,11-didecyldinaphto[2,3-*d*:2′,3′-*d*′]benzo[1,2-*b*:4,5-*b*′]dithiophene), ditbuBTBT (ditert-butyl-[1]-benzothieno-[3,2-*b*]-[1]-1-benzothiophene), and DBTTT (dibenzothiopheno[6,5-*b*:6′,5′-*f*]thieno[3,2-*b*]thiophene), (**Figure 1**). The hole-transporting (p-type) materials examined here exhibit herringbone-type packing, which facilitates efficient charge transport, with ditbuBTBT and DBTTT crystallizing in the monoclinic $P2_1/c$ space group.[24,35,37] C10-DNBDT-NW and C6-DNT-VW deviate from the linear or quasi-linear shape of organic molecules commonly employed in organic semiconductors, and instead are composed of "N" and "V" shaped semiconducting cores, while retaining herringbone packing in the monoclinic $P2_1/c$ and *Pnma* space groups, respectively.[12,13,29] The packing motifs and chemical structures for each of the described materials are illustrated in Figure 1. The choice of these four materials was not only based on their high experimentally-recorded mobilities, but also on the fact that their molecular design could potentially hamper the so-called "killer" phonon mode (i.e., long axis slidings) that is supposed to be responsible for most of the dynamic disorder in herringbone packed materials.[18] generates most of the dynamic disorder in herringbone packing materials: i) the "V"-and "N "-shaped materials exhibit steric hindrance in the solid state along the molecular short axis as a result of the configuration of the aromatic cores,[12] ii) the tbu groups of ditBuBTBT promotes steric hindrance between neighboring molecules of the herringbone layers,[24] and iii) DBTTT is believed to mitigate long-axis sliding motions due to additional S···S interactions between neighboring molecules of the herringbone layers.[35]

While the aforementioned structural modifications of these molecules are generally believed to increase intermolecular wavefunction overlap and suppress low-frequency vibrations in the solid state, the impact of these properties on the underlying electronic factors that enable charge transport remain elusive. Thus, in order to open the investigation of these effects, the experimental measurements of phonons and complementary periodic simulations were performed for each of the described materials, with the experimental cryogenic terahertz absorption spectra,

C. Sawabe
Material Innovation Research Center (MIRC) and Department of Advanced Materials Science, School of Frontier Sciences
The University of Tokyo, 5-1-5 Kashiwanoha
Kashiwa, Chiba 277-8561, Japan

T. Okamoto, J. Takeya
National Institute of Advanced Industrial Science and Technology (AIST)-University of Tokyo Advanced Operando-Measurement Technology Open Innovation Laboratory (OPERANDO-OIL)
AIST, 5-1-5 Kashiwanoha
Kashiwa, Chiba 277-8561, Japan

H. Sirringhaus
Optoelectronics Group, Cavendish Laboratory
University of Cambridge
JJ Thomson Avenue, Cambridge CB3 0HE, UK

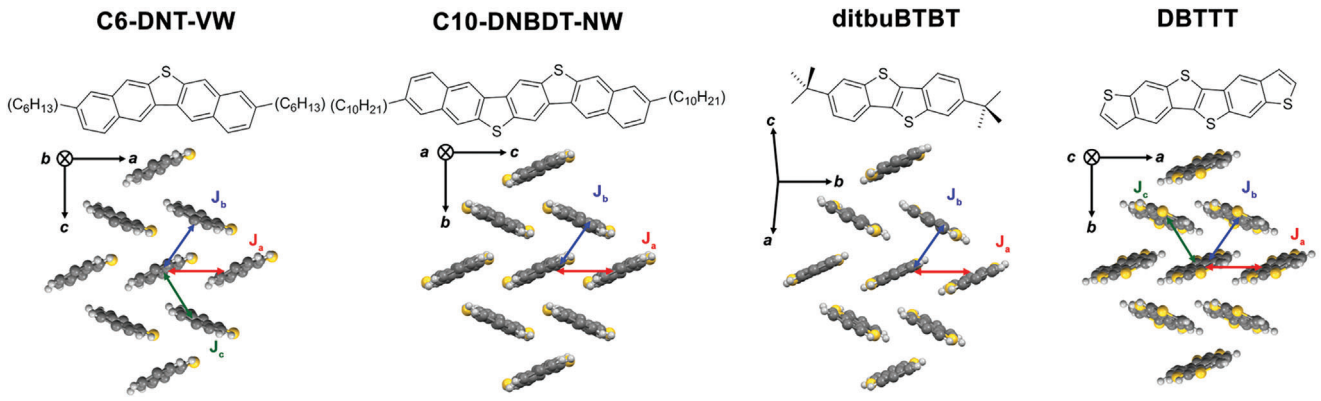

Figure 1. Chemical structures (top) and crystalline packing (bottom) of the studied molecular crystals, with colored arrows and labels (J_x) denoting pairs of molecules that exhibit inequivalent values of the respective charge transfer integral. Alkyl chains substituted from the semiconducting molecular core have been omitted from the crystal structures for clarity.

inelastic neutron scattering (INS) spectra, and theoretical spectra predicted from fully-periodic DFT simulations presented in Figure S2, Supporting Information. Generally, there is good agreement between the theoretical and experimental terahertz spectra with a 90% scaling factor applied to the predicted transition frequencies, which helps account for temperature effects that are neglected under the harmonic approximation.[38,39] Additionally, there is good agreement between the theoretically predicted and experimentally determined unit cell axes (Table S1, Supporting Information), which has been proven to be a useful metric in assessing the accuracy of a periodic simulation.[23] With the theoretical models in good agreement with the experimental data, the predicted normal-modes can be confidently used to evaluate the effects of low-frequency vibrations on charge transport. To first identify the specific mode-types that are most detrimental to charge transport in these systems, transfer integral fluctuations were quantified for each predicted low-frequency vibration, using off-diagonal electron–phonon couplings determined from the dimer projection approach.[18,40–43]

2.1. C6-DNT-VW

The premise that the "V"-shaped molecular core suppresses detrimental vibrational motions in the solid-state, along with high experimentally-recorded hole mobilities (around and above 6.2 $cm^2 V^{-1} S^{-1}$) makes C6-DNT-VW well-suited for a rigorous exploration into the impact that an atypical molecular shape plays on the low-frequency dynamics, as well as the corresponding implications for electronic transport physics. The suppression of large-amplitude molecular motions that hinder charge transport resulting from the steric hinderance of bent molecular cores can quickly be assessed by the frequencies of these vibrational mode-types, such that modes exhibiting high frequencies have reduced vibrational amplitudes, which ultimately reduce transfer integral fluctuations.[18] The calculated fluctuations of transfer integrals for each predicted mode below 400 cm^{-1} for this material are illustrated in **Figure 2**a–c. For this system, two low-frequency modes with vibrational transition frequencies of 15 and 30 cm^{-1}, respectively, exhibit considerable transfer integral fluctuations, and strongly contribute to the thermal energetic disorder arising from Γ-point phonons (Figure 2c). Surprisingly, neither of these modes resemble the strictly asymmetric translational long-axis sliding motion that has been previously demonstrated to exhibit large transfer integral fluctuations.[18] Instead, these modes are composed of rotational motions about the molecular short axis, which produce both symmetric and anti-symmetric motions of molecular dimers throughout the lattice, the latter of which give rise to the large electron–phonon couplings of these vibrations (Figure 2d,e).

While this approach is capable of accurately determining the general role of individual vibrational modes on the thermal

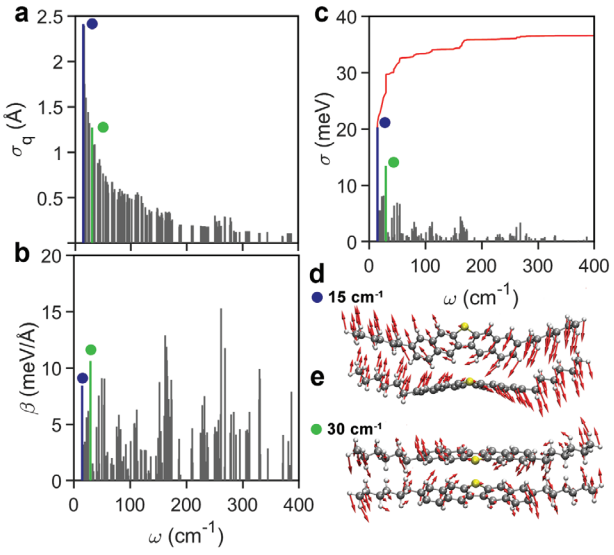

Figure 2. Results of the mode resolved electron–phonon couplings calculated from dimer projection calculations for C6-DNT-VW. a) Mode-amplitudes of vibrations as a function of vibrational transition frequency, b) mode resolved off-diagonal electron–phonon coupling, and c) fluctuation of charge transfer integrals, with a red line illustrating the cumulative total disorder. d, e) Hindered rotational motions of vibrational modes exhibiting large transfer fluctuations, with transition frequencies 15 and 30 cm^{-1}, respectively, with red arrows illustrating atomic displacements. These modes are indicated on (a–c) with blue and green circles, respectively.

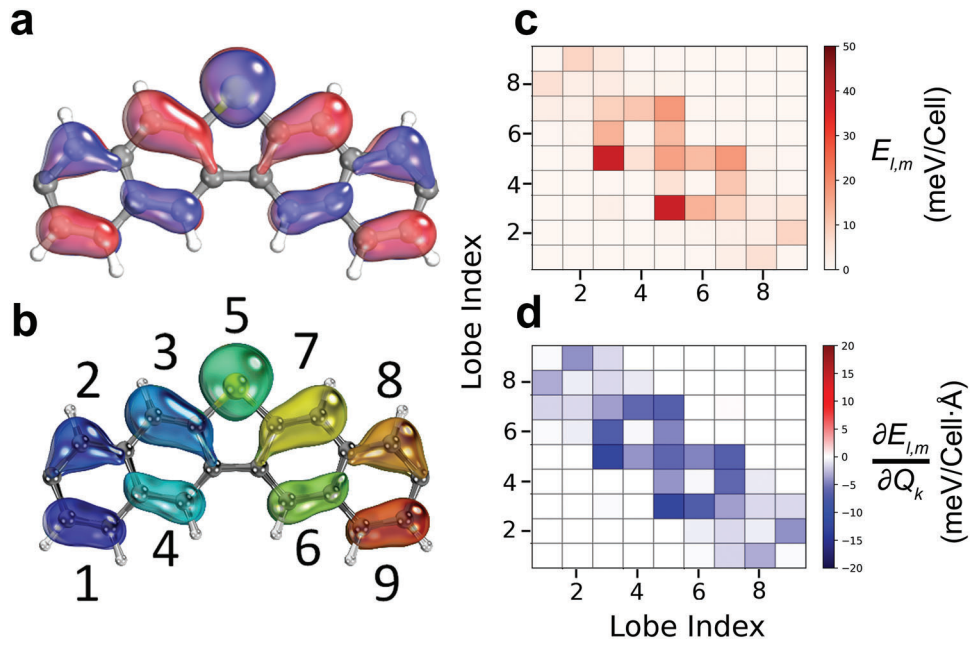

Figure 3. a) HOMO electronic structure and b) COHP labeling scheme of C6-DNT-VW. c) Results of lobe–pair interaction COHP energy determination at equilibrium and d) differentiation with respect to normal mode with vibrational transition frequency 15 cm^{-1}.

energetic disorder, and by extension carrier mobilities, it does not immediately lend insight toward the fundamental electronic factors that ultimately inhibit carrier delocalization. For simple molecular motions, such as vertical displacement of cofacially oriented molecules, these factors are relatively straightforward to analyze and have been historically investigated.[32] However, this analysis is far less intuitive for complex vibrational modes that exhibit many entangled molecular motions, which only becomes further complicated when also considering the specific electronic structure of the molecular orbitals that govern the intermolecular quantum interference. Thus, while the dimer projection approach reveals the unexpected role of complex vibrational modes, such as the hindered-rotational modes described above (Figure 2d,e), the fundamental electronic factors responsible for such findings remain ambiguous, and as such, further examination is required.

For these investigations, COHP analyses offer a powerful means to probe specific intermolecular interactions of crystalline systems with atomic-scale resolution.[44,45] Under the COHP formalism, only selected atomic orbitals from two selected groups of atoms are projected from a specific band (here, the HOMO band) and their interaction calculated, producing a COHP curve (Equation (1)) which upon integration over the band energy interval yields the interaction strength ($E_{l,m}$) of the two selected groups (l, m).[45] In order to carefully inspect the coupling of molecular wavefunctions, atoms of molecules were first grouped according to the regions of the HOMO with consistent phase (i.e., lobes), producing nine discrete lobes, as visualized in **Figure 3**. Integrated COHP values were then calculated for each interaction as a function of the modes described above, for a total of 81 lobe–pair interactions. Ultimately, this treatment yields the relative energies of the specified lobe–pair interactions, as well as their evolution as a function of normal mode displacement. Because of the demonstrated importance of off-diagonal, non-local electron–phonon coupling on carrier mobilities in these systems, we focus this analysis to the intermolecular electronic couplings, though this approach can certainly be extended to investigate local (intramolecular) couplings.

In the case of the "tail-to-tail" molecular dimer (Figure 1, J_c), COHP analysis reveals that the strongest lobe–pair interactions at equilibrium involve the lobes positioned on the molecular center, namely lobes 3, 5, and 7 (Figure 3c), arising from the large HOMO expansion coefficients of the sulfur and alkene carbon atoms, namely a S···π interaction. Such HOMO electronic structures are unique to heteroatom-containing molecules, and as such should be carefully considered when designing improved organic semiconducting materials.[26,46] Additionally, these lobe–pair interactions exhibit the greatest sensitivity to normal coordinate displacement for the vibration with transition frequency 15 cm^{-1}, as illustrated in Figure 3d. Such a result is particularly surprising, given the relatively small normal mode displacement vectors of these atoms with respect to those of the outer-lying groups (Figure 2d). Thus, while it is generally known that the electronic coupling of a molecular dimer is immensely sensitive to its geometry and spatial distribution of the relevant molecular orbital, COHP analysis of this vibration emphasizes that even subtle displacements of specific atoms can strongly modulate key S-π lobe–pair interactions, which can ultimately result in large electron–phonon couplings.

2.2. C10-DNBDT-NW

We now extend this methodology to C10-DNBDT-NW, which like C6-DNT-VW, is composed of an atypical "N" shaped molecular core also designed to suppress vibrational amplitudes, and exhibits high experimentally-recorded hole mobilities (approximately and exceeding 16 $cm^2\,V^{-1}\,S^{-1}$). For this system, two

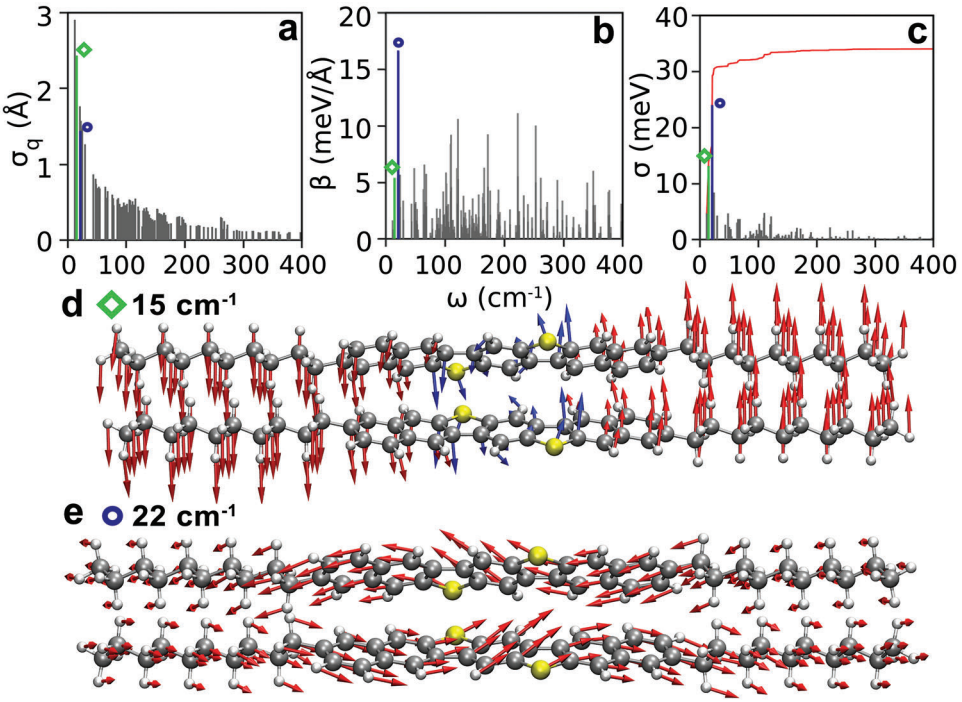

Figure 4. Results of the mode resolved electron–phonon couplings calculated from dimer projection calculations for C10-DNBDT-NW. a) Mode-amplitudes of vibrations as a function of vibrational transition frequency, b) mode resolved off-diagonal electron–phonon coupling, and c) fluctuation of charge transfer integrals, with a red line illustrating the cumulative thermal energetic disorder. d) Hindered translational and e) rotational motions of vibrational modes exhibiting large transfer fluctuations, with transition frequencies 22 and 16 cm^{-1}, respectively, with red arrows illustrating atomic displacements. Blue arrows in (d) have been scaled by a factor of 10 for visual clarity. These modes are indicated on (a–c) with blue circles and green diamonds, respectively.

low-frequency modes with vibrational transition frequencies of 15 and 22 cm^{-1}, respectively, exhibit considerable transfer integral fluctuations, and strongly contribute to the thermal energetic disorder. The mode with transition frequency 22 cm^{-1} is composed of an asymmetric long-axis sliding motion (**Figure 4**e), and exhibits the largest magnitude of both non-local electron–phonon coupling and contribution (≈36%) to the total thermal energetic disorder (Figure 4b,c). This is similar to the findings of our previous study of herringbone-packed p-type organic semiconducting molecular crystals where we referred to this class of motion as a "killer" phonon mode.[18] In contrast, the vibrational mode with transition frequency 15 cm^{-1} has no translational character, and is composed of a symmetric rigid hindered-rotational motion about the molecular short axis (Figure 4d), contributing ≈27% to the thermal energetic disorder. Both the results of the vibrational analysis and non-local electron–phonon couplings for this material are in excellent agreement with the findings of Otaki et al.[28]

While the effects of the long-axis sliding motion on charge transport are expected, the detrimental impacts of the strictly symmetric rotational motion of Figure 4d are surprisingly large, warranting further scrutiny of the vibrational dynamics of this system. COHP analysis of these identified vibrations reveals that like C6-DNT-VW, the strongest lobe–pair interactions of the herringbone-packed molecular dimer are those of the intermolecular S···π interactions restricted to the molecular core (**Figure 5**c), which also exhibit the greatest sensitivity to displacement in the case of both of the aforementioned mode-types. While the broader disruption of lobe–pair interactions involving regions of the entire molecule is expected for the long-axis sliding motion (Figure 5), the rotational mode-type primarily modulates only the core S···π lobe–pair interactions, while again the vibrational displacement vectors are considerably larger along the molecular edges (Figure 4d). Similar to what was found for C6-DNT-VW, this result corroborates the previous finding that even slight disturbances—in this case even symmetric rotational motions—of these central S···π lobe–pair interactions can have severe implications for the modulation of the intermolecular electronic coupling. While the atoms of the outer-lying naphthalene groups have significantly larger displacement vectors for this vibration than those of the benzo[1,2-*b*:4,5-*b*′]dithiophene core, those distal atoms do not interact as strongly with neighboring molecules, reducing their influence. However, this particular mode-type disrupts key proximal lobe–pair interactions, which when predicted with a relatively small transition frequency—and thus a larger thermally-induced displacement amplitude—ultimately produces a large electron–phonon coupling value for this mode.

2.3. ditbuBTBT

The crystalline packing of the C10-DNBDT-NW and C6-DNT-VW materials results in molecular dimers that are directly aligned along the π-stacking coordinate, with the only offset of molecules in this direction arising from the herringbone tilt

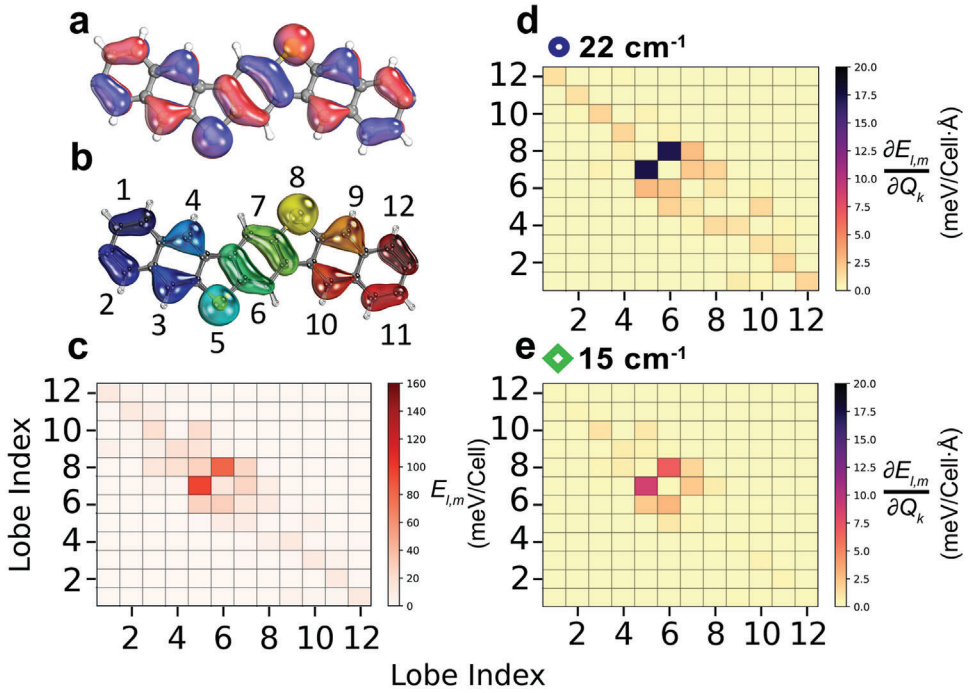

Figure 5. Results of the COHP analysis from solid-state models for C10-DNBDT-NW. a) HOMO electronic structure and b) COHP labeling scheme of C10-DNBDT-NW, with side alkyl chains omitted for clarity. c) Results of lobe–pair interaction COHP energy determination at equilibrium and differentiation with respect to normal mode with vibrational transition frequency d) 22 and e) 15 cm^{-1}. It is important to note that owing to a high degree of crystal symmetry ($Z = 4$), lobe–pair interactions and their derivatives are given as absolute values, as signed values for this system would require prohibitively expensive supercell calculations.

of the molecular dimers. This particular spatial arrangement promotes core–core lobe–pair interactions, as these groups are directly overlaid. Combined with large HOMO expansion coefficients of the proximal atoms, this results in a large disparity between the energies of lobe–pair interactions of the central and peripheral molecular regions. However, in the case of ditbuBTBT, the steric hindrance of the *tert*-butyl groups spatially offsets π-stacked molecules along the molecular long axis, while still retaining herringbone packing. While the linear alkylation of C8-BTBT promotes the asymmetric long-axis sliding as a clear "killer" phonon mode as demonstrated in our previous study, the mode-resolved electron–phonon couplings of ditbuBTBT reveals the presence of several modes that meaningfully contribute to the total energetic disorder, with no one obvious "killer" phonon mode (Figure S8, Supporting Information).[18] Instead, a number of distinct low-frequency vibrational motions exhibit electron–phonon couplings and contributions to the thermal energetic disorder that are similar in magnitude, though the largest transfer integral fluctuation narrowly arises from the asymmetric hindered-translational vibrational motion.

However, while lobes with large HOMO expansion coefficients are contained within the central thieno[3,2-*b*]thiophene unit, the strongest lobe–pair interactions of this material surprisingly exist between these central sulfur orbitals and the lobes of the peripheral benzene moieties (**Figure 6**b, lobes 1 and 5). Such a result arises from the distinct arrangement of molecules in this material, wherein these groups are directly overlaid in the direction of π-stacking. However, while these particular lobe–pairs are promoted by this arrangement, other interactions are undesirably weakened. In this regard, lobe–pairs with restricted spatial overlap are effectively neglected in the overall intermolecular electronic coupling, and exhibit minuscule interaction energies that do not meaningfully evolve along displacement of the hindered-translational mode-type. Consequentially, while the unique set of lobe–pair interactions promote couplings of central and peripheral regions of the molecule (as indicated by the COHP analysis), it also lends the intermolecular electronic interaction vulnerable to other vibrational motions that hinder charge transport, as evidenced by the diverse mode-types with closely similar electron–phonon couplings and transfer integral fluctuations.

2.4. DBTTT

We now extend the COHP methodology to DBTTT, which bears similarities to C10-DNBDT-NW in the quasi-linear molecular shape and inclusion of heteroatoms in the molecular core. However, DBTTT is uniquely constructed with thiophene rings that cap the ends of the molecule, thus incorporating heteratoms along the outer regions of the molecule which is expected to stiffen the intermolecular coordinate. COHP analysis of this system evaluates the role of this design, enabling detailed insight of the influence of these terminal heterocycles on both the electronic structure and dynamic disorder. As seen in the mode-resolved mapping of transfer integral fluctuations (Figure S10, Supporting Information), a number of modes meaningfully contribute to the vibrational disorder, though the largest transfer integral fluctuation expectedly arises from the asymmetric

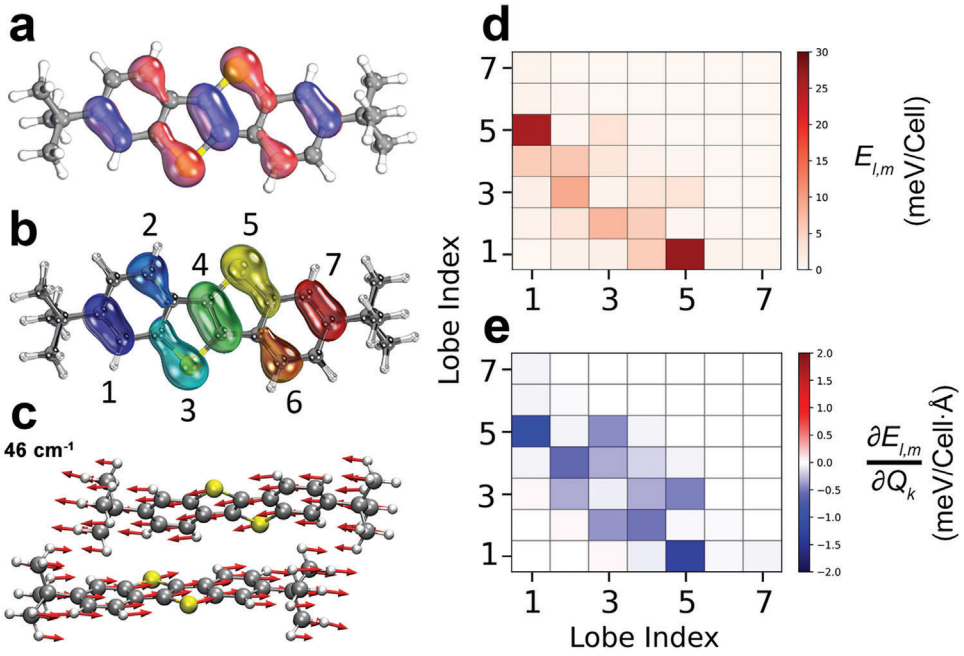

Figure 6. a) HOMO electronic structure and b) COHP labeling scheme of ditbuBTBT. c) Mode-type of vibration with transition frequency 46 cm^{-1}, with red arrows illustrating atomic displacement. d) Results of lobe–pair interaction COHP energy determination at equilibrium and e) differentiation with respect to normal mode with vibrational transition frequency 46 cm^{-1}.

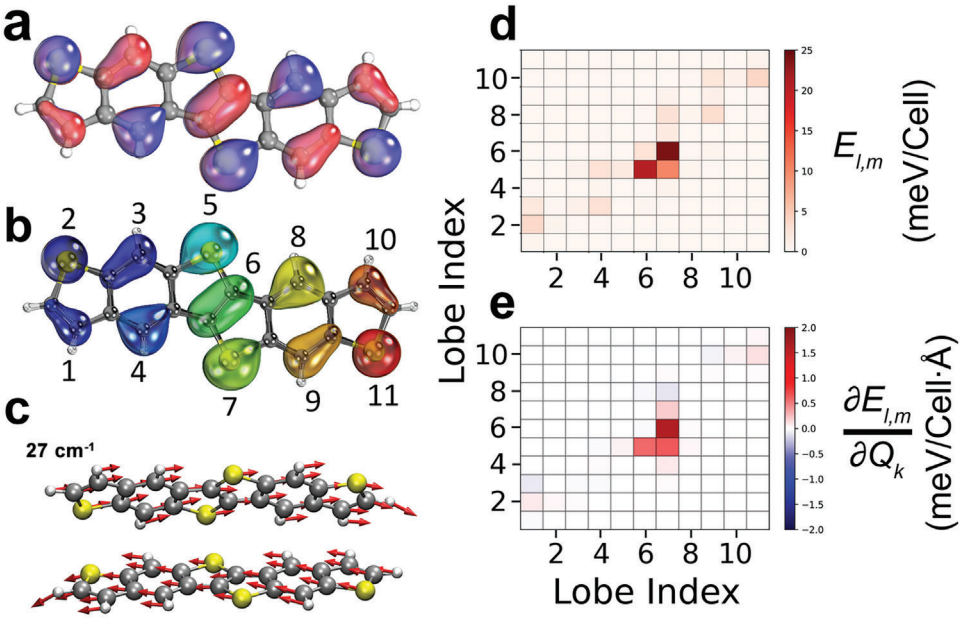

Figure 7. a) HOMO electronic structure and b) COHP labeling scheme of DBTTT. c) Mode-type of vibration with transition frequency 27 cm^{-1}, with red arrows illustrating atomic displacement. d) Results of lobe-pair interaction COHP energy determination at equilibrium and e) differentiation with respect to normal mode with vibrational transition frequency 27 cm^{-1}.

hindered-translational vibrational mode-type. COHP analysis of this mode reveals that the lobe–pair interactions most strongly impacted by this vibrational mode involve the central core lobes of adjacent molecules, specifically those positioned on the sulfur atoms of the central thieno[2,3-*b*]thiophene unit and the C–C bond fusing the two rings (**Figure 7**d lobes 6 and 7), similar to the findings of C10-DNBDT-NW.

Because the terminal sulfur atoms bear significant HOMO expansion coefficients, lobe–pairs involving these groups should be similar in energy to those of the molecular core. However, the HOMO expansion coefficients of carbon atoms positioned along the terminal thiophene rings are comparatively small in

comparison to those of the molecular center, producing relatively weak lobe–pair interactions involving these groups. As a result, these weaker interactions are not meaningfully modulated by the long-axis sliding (Figure 7d). In this regard, the fluctuations of lobe–pair interactions arising from this vibration more closely resembles the effects of the hindered-rotational motion for C10-DNBDT-NW, rather than the related long-axis sliding mode-type, primarily altering core–core lobe–pair interactions. Consequentially, the overall packing of the crystalline system, in tandem with the HOMO electronic structure, points to a negligible role of the outer thiophene rings in the intermolecular electronic coupling.

3. Conclusions

A rigorous exploration into vibrational modes that induce large fluctuations of transfer integrals in a promising set of organic semiconductors was performed, using a multifaceted theoretical and experimental approach. While the dimer projection method has proven a crucial tool for quantifying the impacts of predicted low-frequency vibrational modes, this analysis does not immediately describe the unique manners in which certain vibrations beget these detrimental effects. A thorough comprehension of these effects is highly desirable, as the rich set of low-frequency dynamics exhibited by many molecular crystals consist of highly-entangled molecular motions, which can produce hardly predictable electron– phonon couplings and transfer integral fluctuations. The COHP approach presented here expands upon our previously established theoretical methodology, and further explores the system-specific electronic origins of highly-fluctuating transfer integrals that arise from vibrational motions.

In general, lobes containing atoms with relatively large HOMO expansion coefficients (typically found along the central molecular cores of the thioacenes studied here) are involved in the strongest electronic lobe–pair interactions, which are greatly impacted by low-frequency vibrations, namely the hindered translational and rotational mode-types described here. However, certain structural modifications result in distinct geometric organizations of molecular dimers, in turn favoring new sets of leading lobe–pair interactions. In these cases, more diverse vibrational mode-types induce large transfer integral fluctuations, which are similar to the effects of the known class of asymmetric long-axis sliding motions. While the approach employed here uses Γ-point phonons as a sample of the vibrational dynamics of the investigated systems, this approach can be generalized to full Brillouin zone phonon sampling. Ultimately, the COHP analysis performed here serves to rationalize the manner in which less-commonly studied molecular motions inhibit charge transport. This is a powerful tool for the evaluation of organic semiconductors, suggesting new areas of molecular design that can be exploited to improve charge transport properties in these materials.

Based on these results, a variety of unique molecular modifications purposed to shift detrimental vibrations to higher frequencies result in distinct sets of low-frequency vibrational dynamics. However, in these cases, molecular motions such as the asymmetric parallel long-axis sliding or new vibrational mode-types persist in the low-frequency region, with demonstrable effects on charge transport. While this work emphasizes a number of important factors to consider, the complex interplay between molecular composition, bulk packing, and electronic structure makes the formation of definitive design rules difficult. As such, instead of directly proposing molecular design to hinder the effects of these motions, another aspect of chemical modifications, namely engineering of the charge-transport involved molecular orbitals, may be a more promising avenue for improved optoelectronic materials, which has been the subject of a number of recent reports.[14,47]

4. Experimental Section

Theoretical: All-electron solid-state DFT simulations were performed using the CRYSTAL23 software package.[48,49] All periodic calculations used the GGA PBE density functional[50] along with the Grimme DFT-D3-BJ dispersion correction,[51–53] which wa demonstrated to provide excellent results for molecular crystals,[54] and the split-valence double-zeta def2-SVP basis set.[55] Geometric optimization for each studied crystalline material was performed with no constraints other than maintaining the space group symmetry of the solid, allowing all atoms and lattice vectors to fully relax to an energetic minimum, using a convergence criterion of $\Delta E < 10^{-8}$ hartree. Upon optimization, frequency calculations were performed to produce the vibrational modes, transition frequencies, and IR intensities. The Hessian matrix was calculated as numerical derivatives of the analytic gradients using a three-point formula (i.e., two displacements of 0.001 Å along each Cartesian axis for each atom) which upon diagonalization produces the harmonic Γ-point eigenvalues (vibrational frequencies) and eigenvectors (normal modes).[38,39] Frequency analyses were performed with a more stringent self-consistent field convergence criterion of $\Delta E < 10^{-11}$ hartree. IR intensities were calculated from the Berry phase method, in which first derivatives of the electric polarization are calculated from effective Born tensors expressed over the normal coordinate.[56,57] Due to the previously demonstrated anharmonic nature of ultrasoft vibrational modes,[18] the transition frequencies of all modes less than 0.6 THz (≈20 cm^{-1}) were corrected by an explicit calculation of the anharmonic potential as a function of the normal coordinate. The fundamental anharmonic vibrational transition frequency was calculated through the 1D anharmonic oscillator Schrodinger equation based upon a sixth-order polynomial fit of the potential energy surface.[58] DFT phonon calculations were validated via comparison with INS measurements. INS gave access to all existing modes as it did not suffer from the selection rules present in optical spectroscopy techniques. Additionally, it was highly sensitive to hydrogen motions making it an ideal probe of organic molecules. Such a validation was not only a test of the validity of the underlying structure, but by virtue of the collective nature of the phonons, it served to validate the non-local free energy landscape.[59,60] Theoretical INS spectra were generated using the AbINS software using the solid-state DFT-produced vibrational dynamics.[61]

For C6-DNT-VW, the harmonic frequency calculation yielded negative-frequency modes, indicating that the structure was not optimized to a global minimum. Therefore, the vibrational potentials for the negative-frequency modes were determined by explicitly displacing the structure along the normal coordinate, and calculating the energy at each step. Subsequently, the structure associated with the newly-found energetic minimum was reoptimized. The newly-optimized structure belonged to a different crystalline space group ($P2_1/c$) lower in symmetry than the original one (*Pnma*), which upon frequency analysis produced no imaginary modes.

The influence of vibrational modes on individual intermolecular orbital overlap was investigated using the COHP method. The COHP scheme used here stemed from a generalization of the notion from the orbital-resolved density of states (DOS) and was similar to the crystalline orbital overlap population (COOP) formulation from Hoffman.[62] However, rather than representing the projection of a single orbital or atom projected onto the total electronic DOS, the COHP scheme projects specific

groups (l, m) of atomic orbitals (φ, ν) only to bands (j) of the selected atoms or atomic orbitals (with $\phi \in l$, $\nu \in m$) calculated as

$$\mathrm{COHP}_{l,m}(E) = \frac{2}{V}\sum_{j}\sum_{\phi\in l}\sum_{\nu\in m}\int_{\mathrm{B.Z.}} F_{\phi,\nu}(k)a^{*}_{\phi,j}(k)a_{\nu,j}(k)\delta\left(E - E_j(k)\right)dk \quad (1)$$

With Brillouin zone volume V, reciprocal space coordinate k, Fock matrix $F(k)$, and Bloch coefficients $a_{\phi,j}(k)$. Index j denotes the selected electronic band states, with dispersion relation $E_j(k)$.

It was important to note that in the COHP scheme, the Fock matrix F(k) was used in order to sample over the indexed band structure in reciprocal space, while the overlap matrix S(k) analog constituted the COOP method, which instead of providing the energy of the interaction of groups l and m, detailed the character of the interaction (bonding, antibonding, order).[45,49] In order to ensure consistency with the gas-phase dimer calculations employed for electron–phonon couplings, the COHP analysis relied on crystalline wavefunctions obtained with the more accurate hybrid PBE0[63] functional and the same def2-SVP basis set (vide infa).[55] Reevaluation of the solid-state models in this manner produced electronic structures and relative expansion coefficients in excellent agreement with the gas-phase simulations using the same theoretical parameters. In order to ensure that only the neighboring desired groups for COHP projections were captured, all calculations described in the COHP methodology here used expanded supercells of the crystalline unit cells employed for vibrational analyses.

Because intermolecular electron–phonon (Peierls) couplings were particularly detrimental to change transport for this class of systems with high carrier mobilities, this analysis focused upon off-diagonal, non-local (intermolecular) couplings, rather than the local electron–phonon coupling terms that had previously been demonstrated to be less impactful for charge transport.[10,18,21,31,64] Intermolecular transfer integrals were calculated from the dimer projection approach,[40,41] determined from single point energy calculations performed with the ORCA v4.0 code, employing the PBE0 density functional and def2-SVP basis set[55,65,66] with HOMO–HOMO matrix elements representing transfer integrals for hole transport.[40,41] Sign consistency of each transfer integral was affirmed using "ghost" hydrogenic 1s atomic orbitals to evaluate the phase of the molecular orbitals for each molecule in the given dimer.[66,67] Linear non-local electron–phonon couplings to normal modes were evaluated as the numerical first derivative (determined via central finite differences) of the transfer integral[32] J_x with respect to Cartesian normal-mode coordinate Q_k, calculated as

$$\beta_{x,k} = \left(\frac{\partial J_x}{\partial Q_k}\right)_0 \quad (2)$$

The fluctuations of a given charge transfer integral σ were determined by the product of the non-local coupling $\beta_{x,k}$ and classical thermal vibrational amplitude σ_k^Q

$$\sigma = \beta_{x,k}\,\sigma_k^Q \quad (3)$$

$$[\sigma_k^Q(T)]^2 = \frac{k_B T}{m_k \omega_k^2} \quad (4)$$

With Boltzmann constant k_B, temperature T (evaluated here at 298 K), reduced mass m_k, and vibrational transition frequency ω_k. In the case of any deviation between the anharmonic and harmonic determinations of the vibrational transition frequency, the explicitly determined anharmonic value was used as the corrected transition frequency. Non-local electron–phonon couplings were calculated for each inequivalent dimer in the unit cell. The total disorder arising from lattice vibrations for a given material accounts for fluctuations of each unique transfer integral induced by each predicted vibrational mode. For example, in a system with three unique dimers (a–c) the total vibrational disorder[18] is defined as

$$\sigma = \sqrt{\sigma_a^2 + \sigma_b^2 + \sigma_c^2} \quad (5)$$

Supporting Information

Supporting Information is available from the Wiley Online Library or from the author.

Acknowledgements

M.T.R. and P.A.B. thank the National Science Foundation (DMR-2046483) for financial support. The authors gratefully acknowledge the ISIS neutron and muon source for beam time (TOSCA instrument). G.S. thanks the Belgian National Fund for Scientific Research (FNRS) for financial support through research project COHERENCE2 N. F.4536.23. G.S. is a FNRS Research Associate. G.S. acknowledges financial support from the Francqui Foundation (Francqui Start-Up Grant). G.D. acknowledges financial support from the French "Agence Nationale de la Recherche," project RAPTORS (ANR-21-CE24-0004-01). The authors thank Samsung Electronics for supplying the DBTTT material. The authors thank Samsung Electronics for their support. H.S. acknowledges financial support from the Engineering and Physical Sciences Research Council (EPSRC, Programme Grant EP/W017091/1), the European Research Council (101020872) and the Royal Society (RP\R1\201082).

Conflict of Interest

The authors declare no conflict of interest.

Data Availability Statement

The data that support the findings of this study are available in the supplementary material of this article.

Keywords

density functional theory calculations, electron–phonon coupling, electronic structures, organic semiconductors, vibrational spectroscopy

Received: April 3, 2023
Revised: May 5, 2023
Published online:

[1] K. Kuribara, H. Wang, N. Uchiyama, K. Fukuda, T. Yokota, U. Zschieschang, C. Jaye, D. Fischer, H. Klauk, T. Yamamoto, K. Takimiya, M. Ikeda, H. Kuwabara, T. Sekitani, Y.-L. Loo, T. Someya, *Nat. Commun.* **2012**, *3*, 723.
[2] K. K. Kim, J. Choi, J.-H. Kim, S. Nam, S. H. Ko, K. K. Kim, J. Choi, S. H. Ko, J.-H. Kim, S. Nam, *Adv. Funct. Mater.* **2022**, *32*, 2106329.
[3] S. I. Rich, S. Lee, K. Fukuda, T. Someya, S. I. Rich, K. Fukuda, T. Someya, S. Lee, *Adv. Mater.* **2022**, *34*, 2106683.
[4] T. Someya, T. Sekitani, S. Iba, Y. Kato, H. Kawaguchi, T. Sakurai, *Proc. Natl. Acad. Sci. U. S. A.* **2004**, *101*, 9966.
[5] A. L. Briseno, R. J. Tseng, M. M. Ling, E. H. Falcao, Y. Yang, F. Wudl, Z. Bao, *Adv. Mater.* **2006**, *18*, 2320.

[6] G. Gelinck, P. Heremans, K. Nomoto, T. D. Anthopoulos, *Adv. Mater.* **2010**, *22*, 3778.
[7] Y. Yao, H. Dong, W. Hu, *Adv. Mater.* **2016**, *28*, 4513.
[8] Y. Qian, X. Zhang, L. Xie, D. Qi, B. K. Chandran, X. Chen, W. Huang, *Adv. Mater.* **2016**, *28*, 9243.
[9] A. Troisi, *Chem. Soc. Rev.* **2011**, *40*, 2347.
[10] S. Fratini, M. Nikolka, A. Salleo, G. Schweicher, H. Sirringhaus, *Nat. Mater.* **2020**, *19*, 491.
[11] S. Fratini, S. Ciuchi, D. Mayou, G. T. De Laissardière, A. Troisi, *Nat. Mater.* **2017**, *16*, 998.
[12] T. Okamoto, C. P. Yu, C. Mitsui, M. Yamagishi, H. Ishii, J. Takeya, *J. Am. Chem. Soc.* **2020**, *142*, 9083.
[13] T. Okamoto, C. Mitsui, M. Yamagishi, K. Nakahara, J. Soeda, Y. Hirose, K. Miwa, H. Sato, A. Yamano, T. Matsushita, T. Uemura, J. Takeya, *Adv. Mater.* **2013**, *25*, 6392.
[14] M. Mitani, S. Kumagai, C. P. Yu, A. Oi, M. Yamagishi, S. Nishinaga, H. Mori, Y. Nishihara, D. Hashizume, T. Kurosawa, H. Ishii, N. Kobayashi, J. Takeya, T. Okamoto, *Adv. Electron. Mater.* **2022**, *8*, 2200452.
[15] M. A. Dettmann, L. S. R. Cavalcante, C. A. Magdaleno, A. J. Moul, *Adv. Funct. Mater.* **2023**, 2213370.
[16] K. Takimiya, K. Bulgarevich, M. Abbas, S. Horiuchi, T. Ogaki, K. Kawabata, A. Ablat, K. Takimiya, K. Bulgarevich, S. Horiuchi, T. Ogaki, K. Kawabata, M. Abbas, A. Ablat, *Adv. Mater.* **2021**, *33*, 2102914.
[17] T. F. Harrelson, V. Dantanarayana, X. Xie, C. Koshnick, D. Nai, R. Fair, S. A. Nuñez, A. K. Thomas, T. L. Murrey, M. A. Hickner, J. K. Grey, J. E. Anthony, E. D. Gomez, A. Troisi, R. Faller, A. J. Moulé, *Mater. Horiz.* **2019**, *6*, 182.
[18] G. Schweicher, G. D'Avino, M. T. Ruggiero, D. J. Harkin, K. Broch, D. Venkateshvaran, G. Liu, A. Richard, C. Ruzié, J. Armstrong, A. R. Kennedy, K. Shankland, K. Takimiya, Y. H. Geerts, J. A. Zeitler, S. Fratini, *Adv. Mater.* **2019**, *31*, 1902407.
[19] S. Illig, A. S. Eggeman, A. Troisi, L. Jiang, C. Warwick, M. Nikolka, G. Schweicher, S. G. Yeates, Y. H. Geerts, J. E. Anthony, H. Sirringhaus, *Nat. Commun.* **2016**, *7*, 10736.
[20] A. S. Eggeman, S. Illig, A. Troisi, H. Sirringhaus, P. A. Midgley, *Nat. Mater.* **2013**, *12*, 1045.
[21] M. T. Ruggiero, S. Ciuchi, S. Fratini, G. D'Avino, *J. Phys. Chem. C* **2019**, *123*, 15897.
[22] Y. Krupskaya, M. Gibertini, N. Marzari, A. F. Morpurgo, *Adv. Mater.* **2015**, *27*, 2453.
[23] P. A. Banks, Z. Song, M. T. Ruggiero, *J. Infrared, Millim., Terahertz Waves* **2020**, *41*, 1411.
[24] G. Schweicher, V. Lemaur, C. Niebel, C. Ruzié, Y. Diao, O. Goto, W.-Y. Lee, Y. Kim, J.-B. Arlin, J. Karpinska, A. R. Kennedy, S. R. Parkin, Y. Olivier, S. C. B. Mannsfeld, J. Cornil, Y. H. Geerts, Z. Bao, *Adv. Mater.* **2015**, *27*, 3066.
[25] M. A. Stoeckel, Y. Olivier, M. Gobbi, D. Dudenko, V. Lemaur, M. Zbiri, A. A. Y. Guilbert, G. D'Avino, F. Liscio, A. Migliori, L. Ortolani, N. Demitri, X. Jin, Y.-G. Jeong, A. Liscio, M.-V. Nardi, L. Pasquali, L. Razzari, D. Beljonne, P. Samorì, E. Orgiu, *Adv. Mater.* **2021**, *33*, 2007870.
[26] H. Bronstein, C. B. Nielsen, B. C. Schroeder, I. McCulloch, *Nat. Rev. Chem.* **2020**, *4*, 66.
[27] S. E. Root, S. Savagatrup, A. D. Printz, D. Rodriquez, D. J. Lipomi, *Chem. Rev.* **2017**, *117*, 6467.
[28] T. Otaki, T. Terashige, J. Tsurumi, T. Miyamoto, N. Kida, S. Watanabe, T. Okamoto, J. Takeya, H. Okamoto, *Phys. Rev. B* **2020**, *102*, 245201.
[29] C. Mitsui, T. Okamoto, M. Yamagishi, J. Tsurumi, K. Yoshimoto, K. Nakahara, J. Soeda, Y. Hirose, H. Sato, A. Yamano, T. Uemura, J. Takeya, *Adv. Mater.* **2014**, *26*, 4546.
[30] C. Liu, J. Yang, J. Xi, X. Ke, *Nanoscale* **2019**, *11*, 10828.
[31] S. Fratini, D. Mayou, S. Ciuchi, *Adv. Funct. Mater.* **2016**, *26*, 2292.
[32] V. Coropceanu, J. Cornil, D. A. da Silva Filho, Y. Olivier, R. Silbey, J. L. Brédas, *Chem. Rev.* **2007**, *107*, 926.
[33] A. Troisi, G. Orlandi, *Phys. Rev. Lett.* **2006**, *96*, 086601.
[34] T. Nematiaram, A. Troisi, *J. Chem. Phys.* **2020**, *152*, 190902.
[35] J. I. Park, J. W. Chung, J. Y. Kim, J. Lee, J. Y. Jung, B. Koo, B. L. Lee, S. W. Lee, Y. W. Jin, S. Y. Lee, *J. Am. Chem. Soc.* **2015**, *137*, 12175.
[36] A. Y. Sosorev, D. R. Maslennikov, I. Y. Chernyshov, D. I. Dominskiy, V. V. Bruevich, M. V. Vener, D. Y. Paraschuk, *Phys. Chem. Chem. Phys.* **2018**, *20*, 18912.
[37] H. Sirringhaus, *Adv. Mater.* **2014**, *26*, 1319.
[38] F. Pascale, C. M. Zicovich-Wilson, F. López Gejo, B. Civalleri, R. Orlando, R. Dovesi, *J. Comput. Chem.* **2004**, *25*, 888.
[39] C. M. Zicovich-Wilson, F. Pascale, C. Roetti, V. R. Saunders, R. Orlando, R. Dovesi, *J. Comput. Chem.* **2004**, *25*, 1873.
[40] B. Baumeier, J. Kirkpatrick, D. Andrienko, *Phys. Chem. Chem. Phys.* **2010**, *12*, 11103.
[41] E. F. Valeev, V. Coropceanu, D. A. Da Silva Filho, S. Salman, J. L. Brédas, *J. Am. Chem. Soc.* **2006**, *128*, 9882.
[42] A. Girlando, L. Grisanti, M. Masino, I. Bilotti, A. Brillante, R. G. Della Valle, E. Venuti, *Phys. Rev. B* **2010**, *82*, 035208.
[43] A. Girlando, L. Grisanti, M. Masino, A. Brillante, R. G. Della Valle, E. Venuti, *J. Chem. Phys.* **2011**, *135*, 84701.
[44] R. Dronskowski, P. E. Blöchl, *J. Phys. Chem.* **1993**, *97*, 8617.
[45] M. T. Ruggiero, A. Erba, R. Orlando, T. M. Korter, *Phys. Chem. Chem. Phys.* **2015**, *17*, 31023.
[46] K. Takimiya, S. Shinamura, I. Osaka, E. Miyazaki, *Adv. Mater.* **2011**, *23*, 4347.
[47] A. Yamamoto, Y. Murata, C. Mitsui, H. Ishii, M. Yamagishi, M. Yano, H. Sato, A. Yamano, J. Takeya, T. Okamoto, *Adv. Sci.* **2018**, *5*, 1700317.
[48] A. Erba, J. Baima, I. Bush, R. Orlando, R. Dovesi, *J. Chem. Theory Comput.* **2017**, *13*, 5019.
[49] R. Dovesi, A. Erba, R. Orlando, C. M. Zicovich-Wilson, B. Civalleri, L. Maschio, M. Rérat, S. Casassa, J. Baima, S. Salustro, B. Kirtman, *WIREs Comput. Mol. Sci.* **2018**, *8*, e1360.
[50] J. P., Perdew, K. Burke, M. Ernzerhof, *Phys. Rev. Lett.* **1996**, *77*, 3865.
[51] D. G. Smith, L. A. Burns, K. Patkowski, C. D. Sherrill, *J. Phys. Chem. Lett.* **2016**, *7*, 2197.
[52] S. Grimme, S. Ehrlich, L. Goerigk, *J. Comput. Chem.* **2011**, *32*, 1456.
[53] S. Grimme, *WIREs Comput. Mol. Sci.* **2011**, *1*, 211.
[54] N. Bedoya-Martínez, A. Giunchi, T. Salzillo, E. Venuti, R. G. Della Valle, E. Zojer, *J. Chem. Theory Comput.* **2018**, *14*, 4380.
[55] F. Weigend, R. Ahlrichs, *Phys. Chem. Chem. Phys.* **2005**, *7*, 3297.
[56] Y. Noel, C. M. Zicovich-Wilson, B. Civalleri, P. D'Arco, R. Dovesi, *Phys. Rev. B* **2002**, *65*, 014111.
[57] R. Dovesi, B. Kirtman, L. Maschio, J. Maul, F. Pascale, M. Rérat, *J. Phys. Chem. C* **2019**, *123*, 8336.
[58] M. Hutereau, P. A. Banks, B. Slater, J. A. Zeitler, A. D. Bond, M. T. Ruggiero, *Phys. Rev. Lett.* **2020**, *125*, 103001.
[59] J. Armstrong, A. J. O'Malley, M. R. Ryder, K. T. Butler, *J. Phys. Commun.* **2020**, *4*, 072001.
[60] J. Armstrong, S. Banerjee, V. Schünemann, J. A. Wolny, P. J. Sadler, *J. Phys. Chem. Lett.* **2021**, *12*, 658.
[61] K. Dymkowski, S. F. Parker, F. Fernandez-Alonso, S. Mukhopadhyay, *Phys. B. Condens. Matter* **2018**, *551*, 443.
[62] T. Hughbanks, R. Hoffmann, *J. Am. Chem. Soc.* **1983**, *105*, 3528.
[63] C. Adamo, V. Barone, *J. Chem. Phys.* **1999**, *110*, 6158.
[64] S. Fratini, S. Ciuchi, *Phys. Rev. Res.* **2020**, *2*, 013001.
[65] J. P. Perdew, M. Ernzerhof, K. Burke, *J. Chem. Phys.* **1996**, *105*, 9982.
[66] F. Neese, *WIREs Comput. Mol. Sci.* **2012**, *2*, 73.
[67] J. Li, G. D'Avino, I. Duchemin, D. Beljonne, X. Blase, *Phys. Rev. B* **2018**, *97*, 35108.